Support Information

Size-tunable MoS_2 nanosheets for controlling crystal morphology and residual stress in sequential-deposited perovskite solar cells over 22.5% efficiency

Zhanfei Zhang[1], *Jianli Wang*[1], *Lizhong Lang*, *Yan Dong*, *Jianghu Liang*, *Yiting Zheng*, *Xueyun Wu*, *Congcong Tian, Ying Huang*, *Zhuang Zhou*, *Yajuan Yang*, *Luyao Wang*, *Lingti Kong*, *Chun-Chao Chen**

Experiment

Materials

Ammonium molybdate ($(NH_4)_6Mo_7O_{24}\cdot 4H_2O$), Sodium ethyl xanthate ($C_2H_5OC(=S)SNa$) and Ammonia ($NH_3\cdot H_2O$) were purchased from Macklin. N,N-Dimethylformamide (DMF, 99.8%), Dimethyl sulfoxide (DMSO, 99.8%), acetonitrile (ACN), 4-*tert*-butylpyridine (4-tBP, 98%), isopropanol (IPA), chlorobenzene (CB) were obtained from Sigma-Aldrich. Lead (II) iodide (PbI_2, >99.99%), Formamidinium Iodide (FAI, >99.5%), Methylammonium Bromide (MABr, >99.5%), Methylammonium Chloride (MACl, >99.5%), 2,2',7,7'-tetrakis-(N,N-di-pmethoxyphenylamine)-9,9'-spirobifluorene (Spiro-OMeTAD, 99%) and lithium bis (trifluoromethylsulfonyl)imide (Li-TFSI, 95%) were acquired from Xi'an Polymer Light Technology Crop. SnO_2 colloid solution (tin (iv) oxide, 15% in H_2O colloidal dispersion) was purchased from Alfa Aesar. All these materials were used as received.

MoS_2 nanosheets preparation

0.25 g $(NH_4)_6Mo_7O_{24}\cdot 4H_2O$ and 0.55 g $C_2H_5OC(=S)SNa$ were dissolved in 30 mL deionized water respectively. A few drops of ammonia were added to adjust the pH of the molybdenum solution to 6.00. Then mixing these two solutions and magnetically stirred for 20 min, transferred them to a Teflon-lined stainless autoclave, and maintained at 200 °C for 8 h. After the reactor was cooled to room temperature naturally, the reaction products were collected by centrifugation with different centrifugal rates of 3000, 6000, and 9000 rpm min^{-1}, washed with deionized water and absolute ethanol several times. The precipitation was dried in a blast drying oven to obtain black MoS_2 powders.

MoS_2 doped PbI_2 precursor solution preparation

2 mg of MoS_2 powders was dissolved in 2 mL of DMSO:DMF=1:9 mixed solvent and ultrasonically dispersed at room temperature for 20 min, the well-dispersed MoS_2 solution (1 mg/mL) with Tyndall effect are shown in Figure S17 respectively. Then the certain amount of MoS_2 solution was pipetted into the PbI_2 precursor solution, the mixed precursor solution was magnetically stirred at the room temperature for 5 h. Finally, the MoS_2 doped PbI_2 precursor solution was prepared and waiting for the spin-coating process.

Perovskite solar cells fabrication

The glass/FTO substrates were sequentially washed with deionized water, absolute ethanol, acetone, and isopropanol in the ultrasonic bath for 20 min. Then, FTO substrates were further cleaned via UV-Ozone treatment for 15 min. After cooling down to room temperature, diluted SnO_2 nanoparticles (2.67%, in deionized water) solution was spin-coated on FTO substrates at 3000 rpm for 30 s and annealed at 180 °C for 30 min in ambient air. Then placed the SnO_2 substrates in ultraviolet ozone for 10 min to improve its wettability. After depositing the electron transport layer, the perovskite layer was fabricated by a two-step spin coating method in the glove box. Firstly, PbI_2 (1.3 M of PbI_2 in DMSO:DMF=1:9) modifying with different sizes of MoS_2 solution was spin-coated on SnO_2 substrates at 1500 rpm for 30 s and annealed at 70 °C for 60 s. After the PbI_2 cooled down, the mixed organic-inorganic precursor solution (CsI 30 mg, FAI 60mg, MABr 6 mg, and MACl 6 mg were dissolved in 1 mL isopropanol) was coated onto the PbI_2 film at 1500 rpm for 30 s, then the film was taken out of the glove box and annealed at 170 °C for 20 min in ambient air with the humidity of 30%~40%. Then the grown perovskite film had been transferred in the glove box, the spiro-OMeTAD hole transport layer, which consisted of 72.3 mg spiro-OMeTAD, 45 μL LiTFSI solution (260 mg LiTFSI in 1 mL acetonitrile), 30 μL 4-tBP, and 1 mL chlorobenzene, was coated onto the perovskite layer at 1500 rpm for 30 s. Finally, an Ag back electrode was thermally evaporated on the device through a shallow mask at the pressure of 9×10^{-5} Pa. The effective area of the electrode was 0.1 cm^2. All device measurements were unencapsulated and performed in ambient air with the humidity under 30 ± 5% at room temperature.

Characterization

The J-V characteristics of the as-prepared devices were tracked by a Keithley 2400 source measurement under a simulated AM 1.5G spectrum at 100 mW/cm^2 (Abet Technologies Sun 2000 solar simulator, calibrated with a standard VLSI Si reference solar cell (SRC-1000-TC-K-QZ), including reverse scanning ranges from 1.2 V to -0.2 V with an interval of 20 mV/s and forward scanning ranges from -0.2 V to 1.2 V with the same steps. The external quantum efficiency (EQE) spectra were recorded by the QTEST HIFINITY 5 EQE system (the light intensity was calibrated with Si detectors) in ambient air. Filed emission scanning electron microscopy (FESEM) images were acquired on RISE-MAGNA FE-SEM. Steady-state photoluminescence (PL) and time-resolved photoluminescence (TRPL) were conducted by FLS 1000 photoluminescence spectrometer by a light incident from the perovskite film side and the excitation wavelength was 470 nm. Uv-vis absorption spectra were recorded by Lambda 35 Uv-vis spectrometer. X-ray photoelectron spectra (XPS) analyses were carried out using a Thermo Scientific K-alpha X-ray photoelectron spectrometer and calibrated with C1s binding energy. Electrochemical impedance spectroscopy (EIS) spectra were observed on a Chenhua CHI660E electrochemical workstation under dark conditions. The grazing incidence wide-angle X-ray scattering (GIWAXS) spectra were obtained at beamline BL16B1 in the Shanghai Synchrotron Radiation Facility (SSRF) and the incidence angle of the X-ray beam was 0.3 °, The normal incidence of Shanghai Synchrotron Radiation Facility (SSRF) 16B is about 400 microns, and the grazing incidence spot can reach the centimeter-level (grazing incidence angle of 0.3 °, the spot along the optical path can be elongated to 400/sin°(0.3°)=7.6 cm, with a spot area around 400 μm × 7.6 cm). Thus, the surface effect is magnified. Atomic force microscopy (AFM) images were observed on a Bruker Bio-FastScan AFM.

Surface Residual Stress Measurements

X-ray diffraction (XRD) patterns were detected with a Bruker D8 Advance X-ray diffractometer under Cu Kα radiation and 8-60° scan range with a step size of 0.02 °/s. Diffraction patterns were collected as a function of the θ angle of the thin film, using two different orthogonal orientations (Φ=0 and 90°) for confirming the isotropic nature of the residue stresses. The d spacings (012) for the well-defined XRD peaks at the highest 2θ angle (~31.6°) were used to generate the $\sin^2\psi$ plots. (012) interplanar spacing (d_{012}) is plotted as a function of $\sin^2\psi$ for perovskite film modifying with different sizes of MoS_2 nanosheets. The biaxial residual stress (σ_R) can be estimated from the $\sin^2\psi$ data using the following relation:[1]

$$\sigma_R = (\frac{E_{(012)}}{1+\nu})(\frac{m}{d_n})$$

Where m is the slope of the linear fit to the data, d_n is the d_{012} spacing at $\sin^2\psi=0$ (y-intercept), $E_{(012)}$ is Young's modulus in the (012) direction, v is the Poisson ratio. The $E_{(012)}$ of perovskite is estimated as 10 Gpa.[2,3] The typical v valve of 0.3 is estimated.[4]

Density functional theory (DFT) calculations

We performed density functional theory (DFT) based first-principle calculation: We implemented Vienna Ab initio Simulation Package (VASP) code by using the projector-augmented wave (PAW) method. We adopted Perdew-Burke-Ernzerh's (PBE) exchange-correlation functional within the generalized gradient approximation (GGA). DFT-D3 method of Grimme is also applied to correct van der Waals (vdW) interaction. The electron wave function basis set was expanded up to cutoff energy of 500 eV. A 4×4×1 Monkhorst. Pack (MP) k mesh with a gamma k-point was adopted. For $MAPbI_3$ (001)/MoS_2 absorption, a 15 Å vacuum layer is adopted to avoid the interaction between neighboring slabs. The convergence standard is set at 0.02 eV Å^{-1} for the total force of each atom, and the convergence threshold of energy for each atom is less than 1×10^{-5} eV. The dipole correction is calculated parallel to the z-direction, and the potential correction mode (the LDIPOL tag) was also switched on to counterbalance the local potential and the force errors introduced by the periodic boundary conditions.

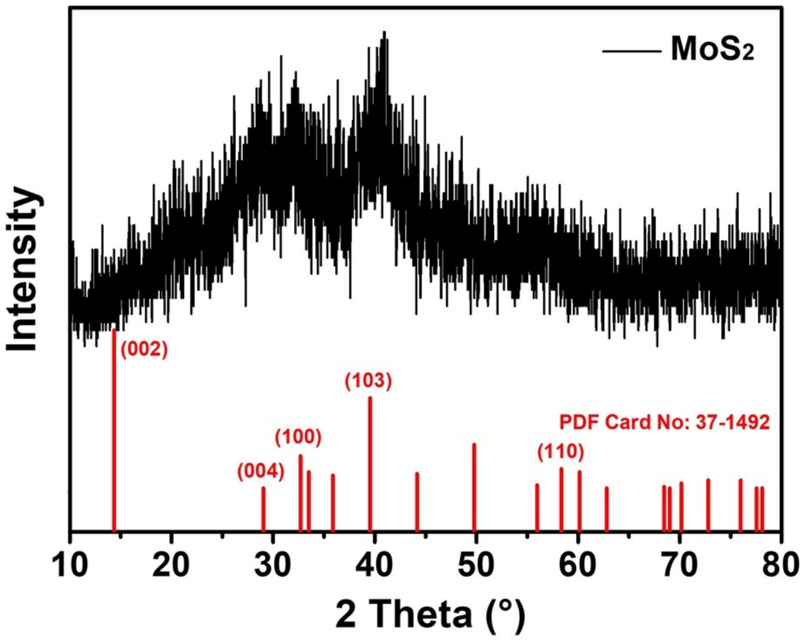

Fig. S1 The XRD pattern of as-prepared MoS_2 nanosheets.

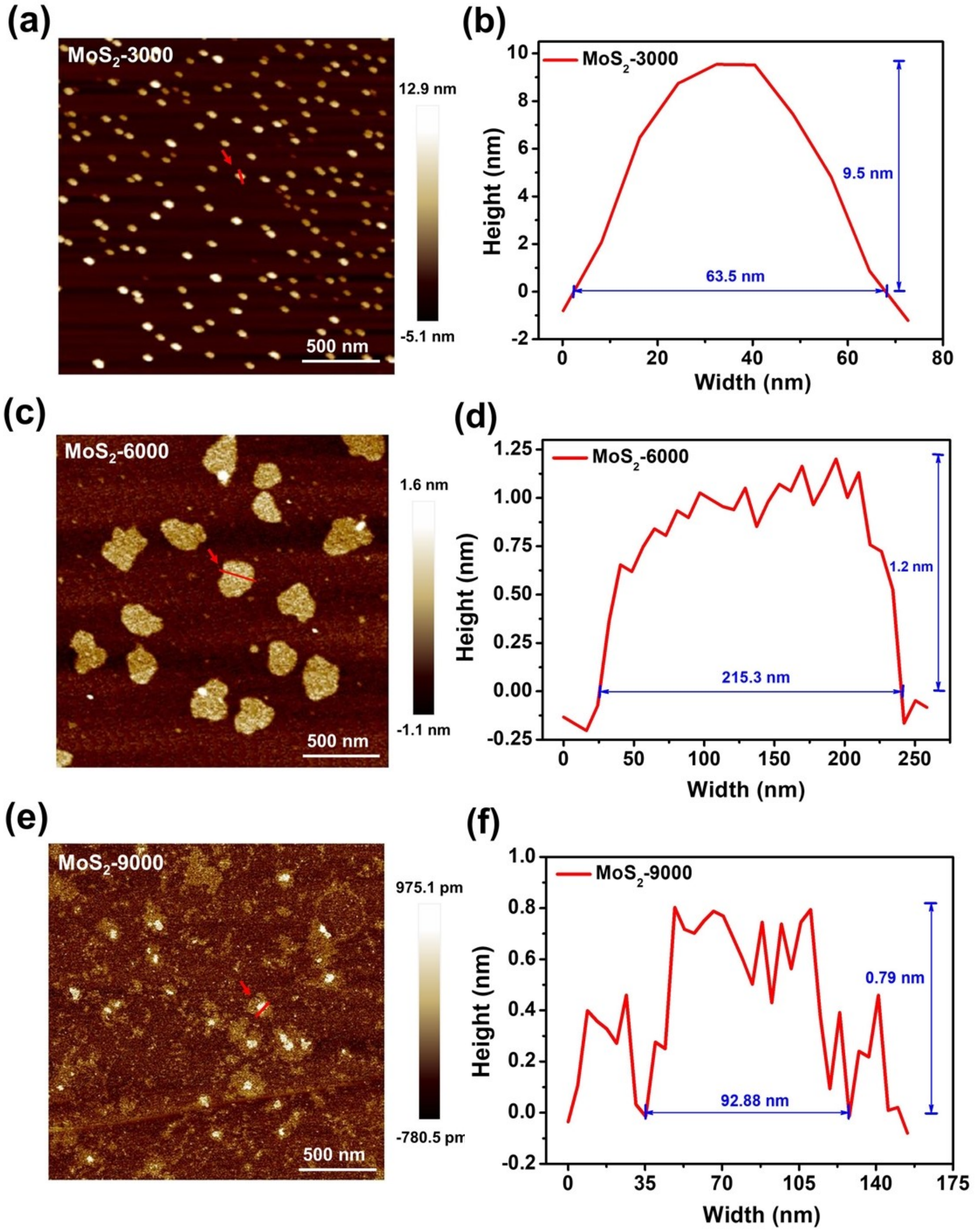

Fig. S2 Representative AFM images of the as-prepared MoS$_2$: (a) MoS$_2$-3000 nanosheets, (c) MoS$_2$-6000 nanosheets and (e) MoS$_2$-9000 nanosheets; their corresponding height profiles (b), (d) and (f) for the AFM section lines as list in (a), (c) and (e).

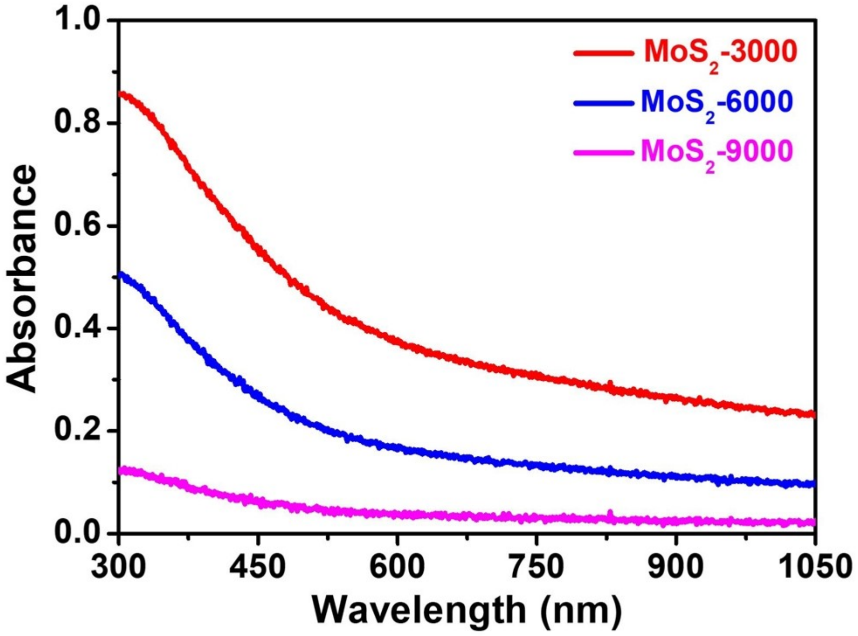

Fig. S3 The optical absorption spectra of MoS_2 solution with different separation centrifugal speed (3000, 6000 and 9000 rpm/min).

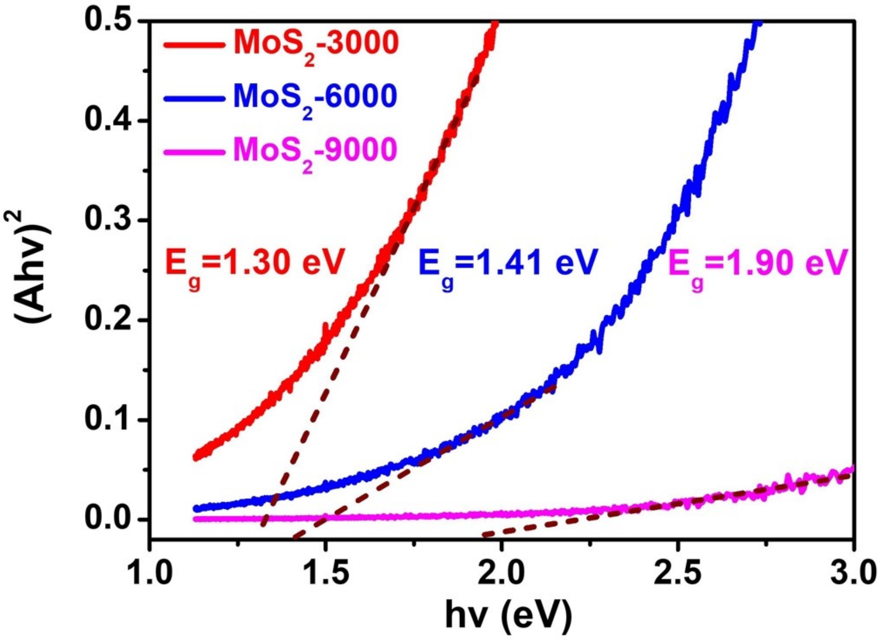

Fig. S4 The relationship of $(Ahv)^2$ vs (hv) for MoS_2 nanosheets with different separation centrifugal speeds (3000, 6000, and 9000 rpm/min). The bandgap (E_g) of different thickness MoS_2 nanosheets can be determined via linear exploration of the leading edges of the $(Ahv)^2$ curve to the baselines

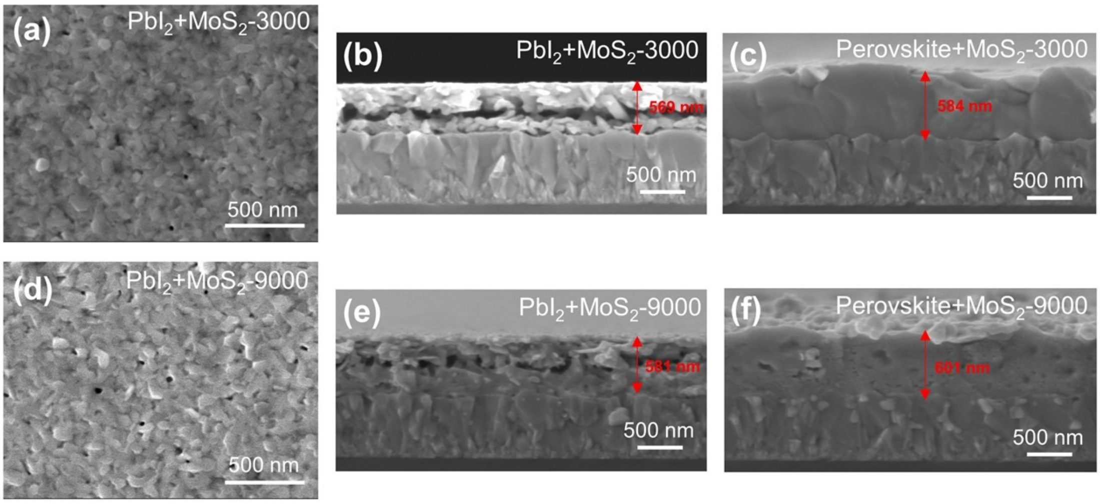

Fig. S5 Top-view SEM images of the MoS$_2$-3000 (a) and the MoS$_2$-9000 modified PbI$_2$ film (d) deposited on SnO$_2$; Cross-sectional SEM images of the MoS$_2$-3000 modified PbI$_2$ film (b) and corresponding perovskite film (c), the MoS$_2$-9000 modified PbI$_2$ film (e) and corresponding perovskite film (f) deposited on SnO$_2$.

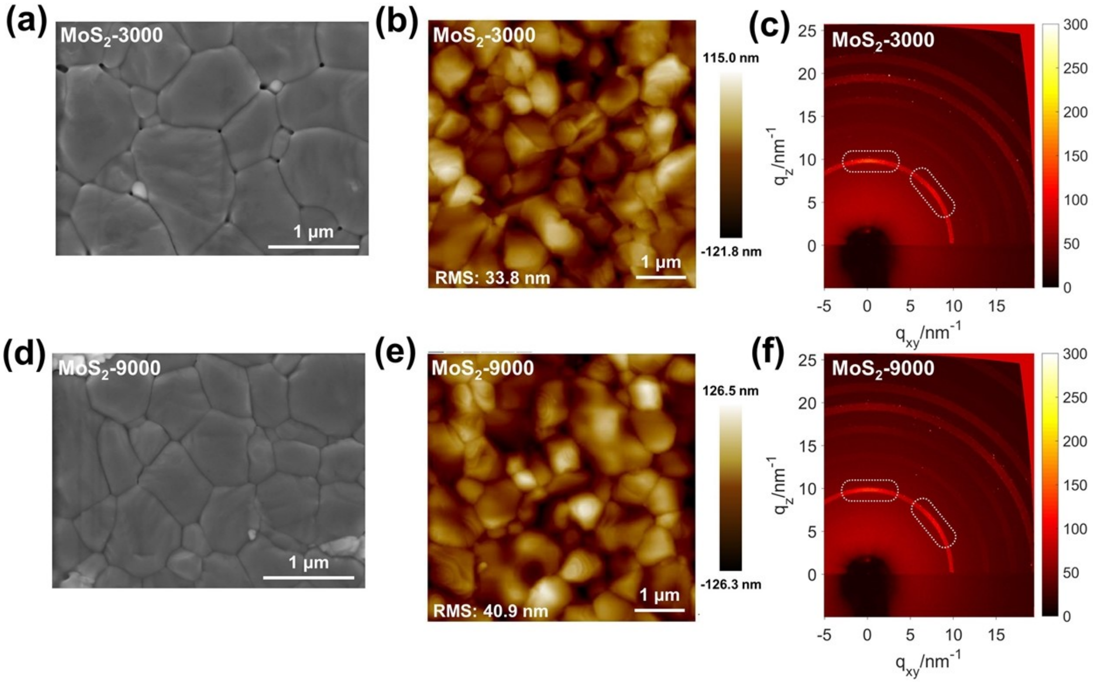

Fig. S6 Top view (a) (d) SEM images, (b) (e) AFM images, and (c) (f) GIWAX patterns of perovskite films.

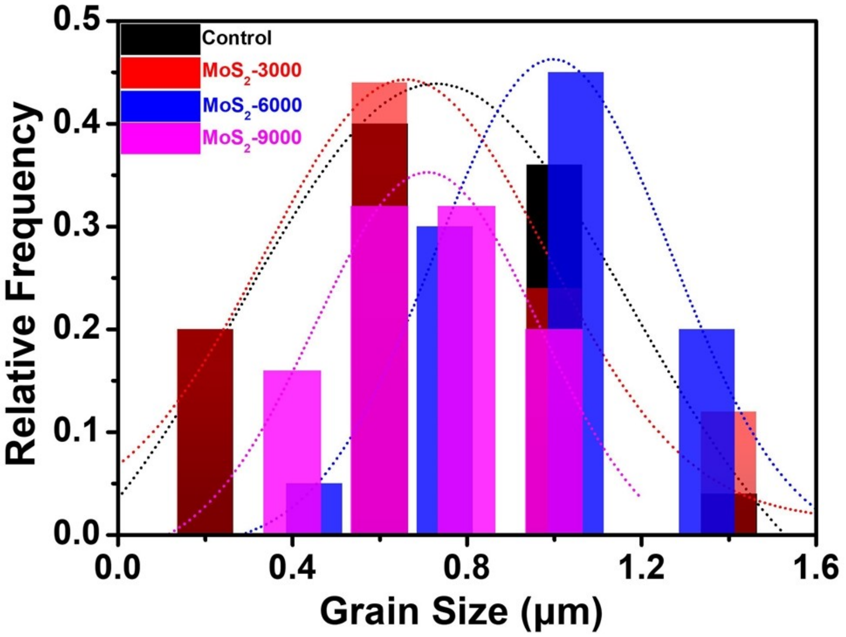

Fig. S7 The comparison of grain size distribution for perovskite film.

Control : Mean 0.70 μm; MoS_2-3000 : Mean 0.72 μm;

MoS_2-6000 : Mean 0.99 μm; MoS_2-9000 : Mean 0.72 μm

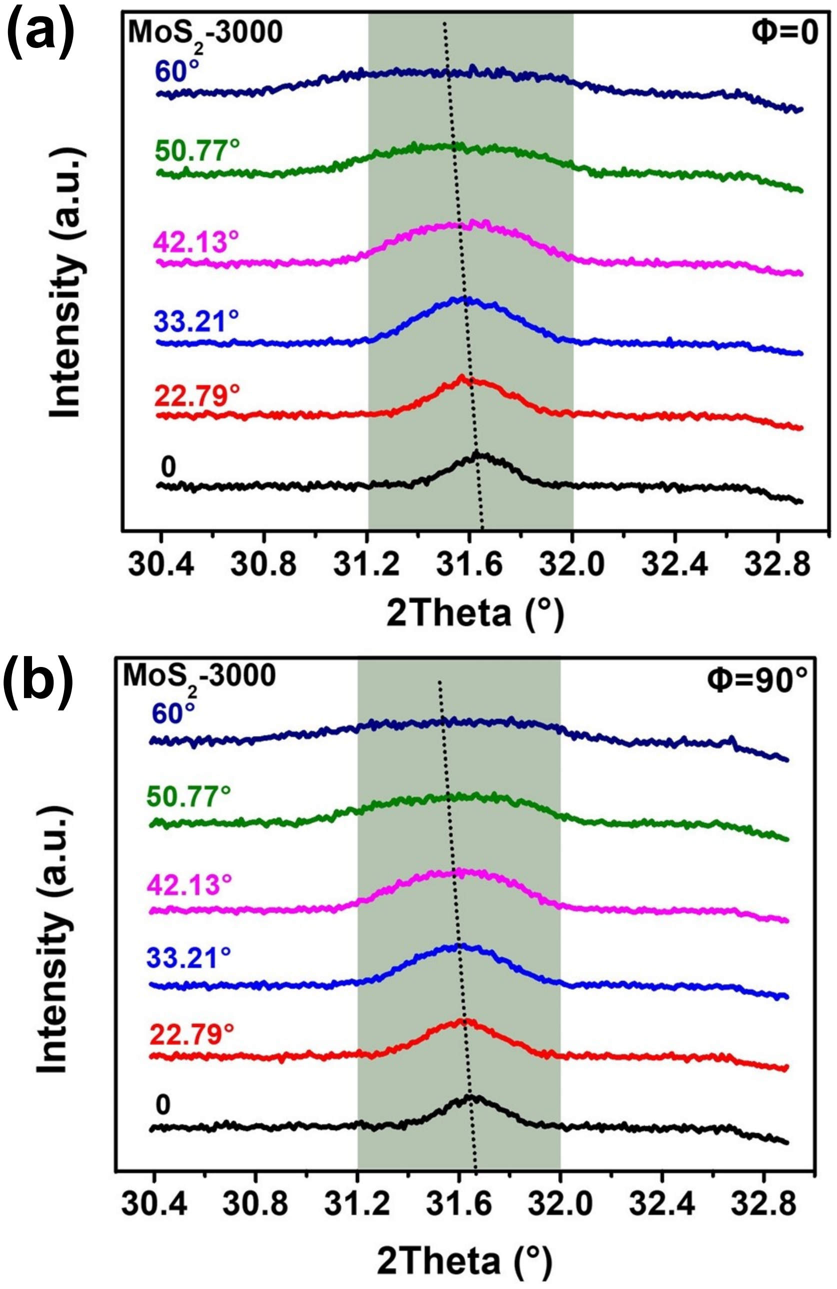

Fig. S8 XRD spectra of magnified (012) lattice plane diffraction peaks under different Φ values for perovskite film modified with MoS_2-6000 nanosheets: (a) Φ=0 and (b) Φ=90 °.

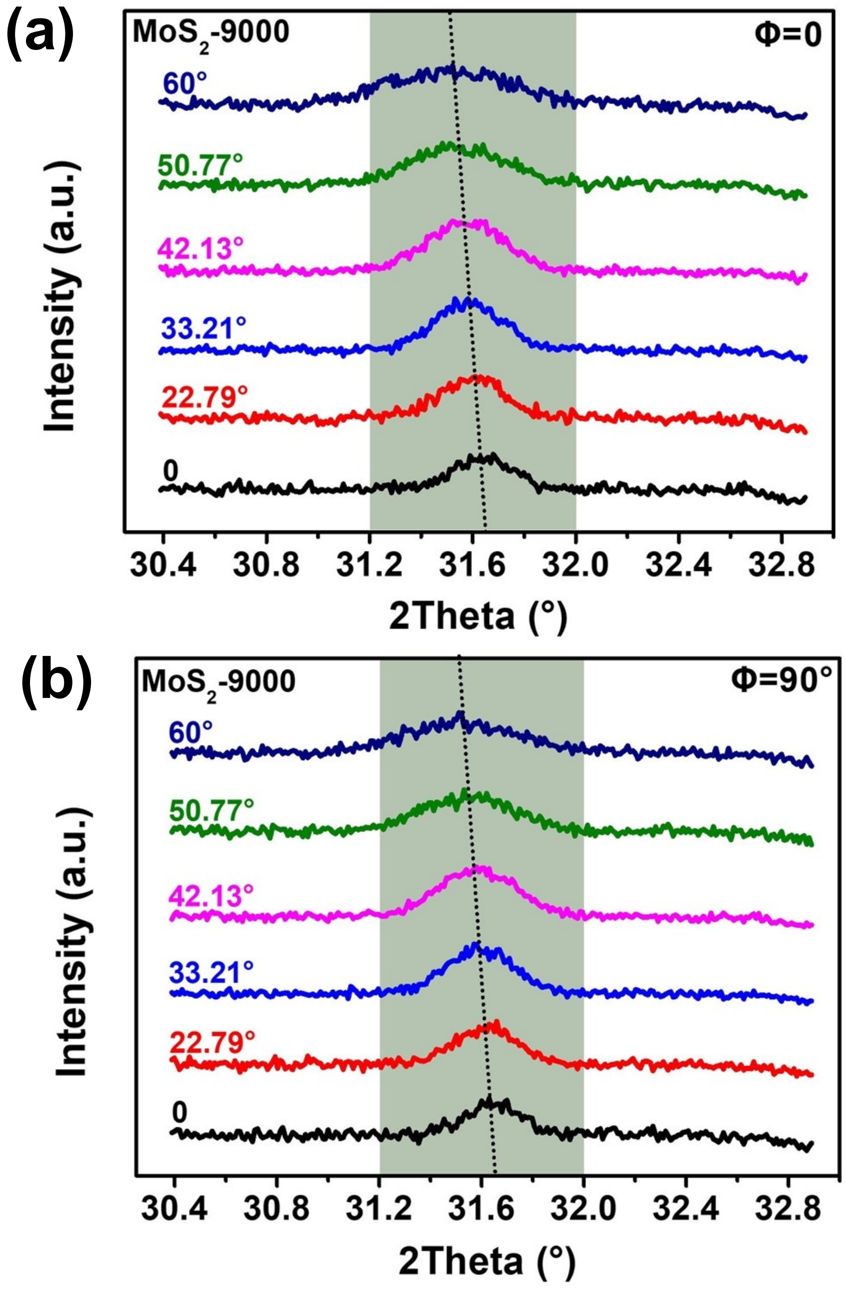

Fig. S9 XRD spectra of magnified (012) lattice plane diffraction peaks under different Φ values for perovskite film modified with MoS_2-9000 nanosheets: (a) Φ=0 and (b) Φ=90 °.

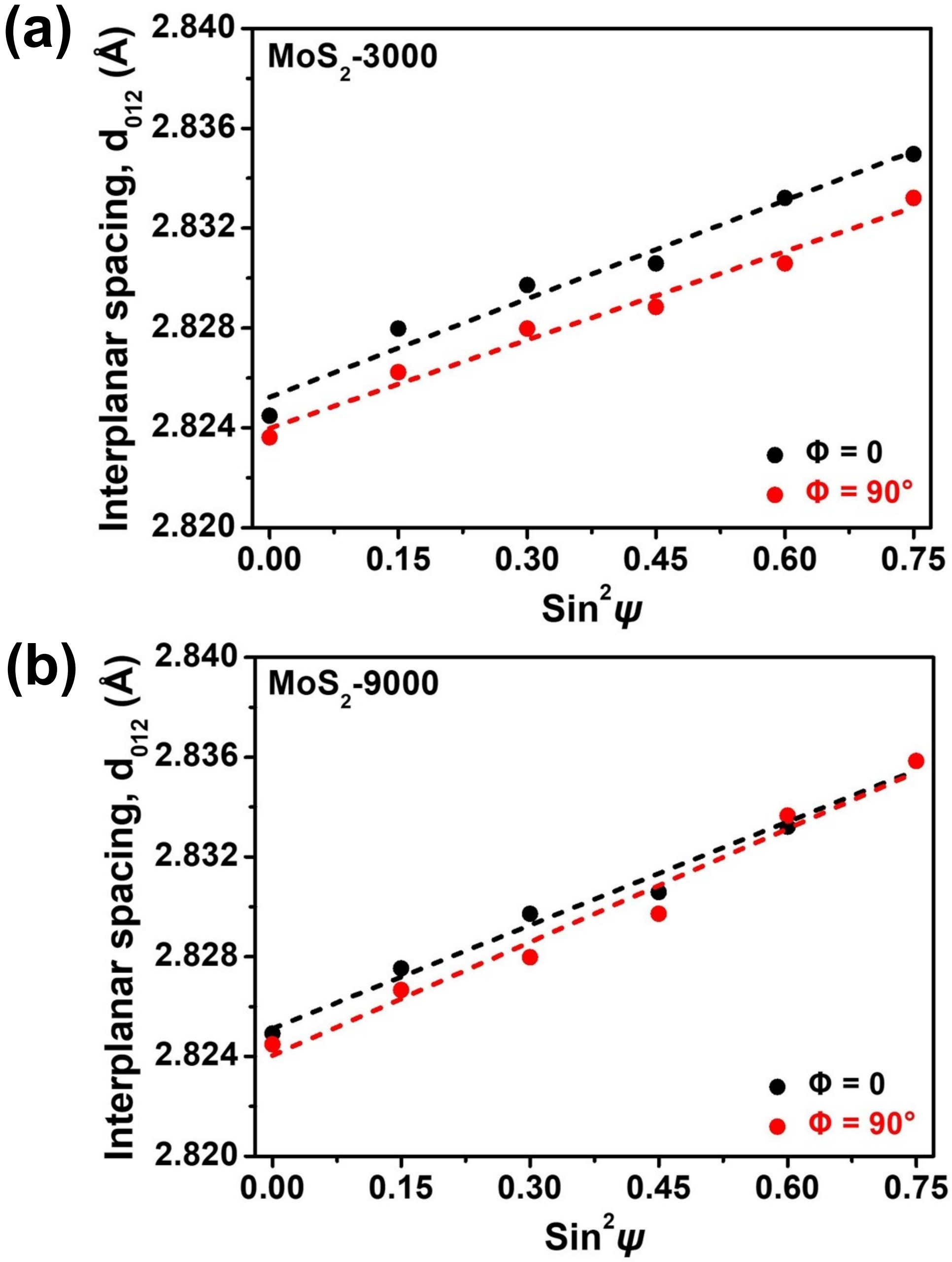

Fig. S10 XRD d_{012} versus $\sin^2\Psi$ plots for perovskite film modified with MoS_2-3000 and MoS_2-9000 nanosheets.

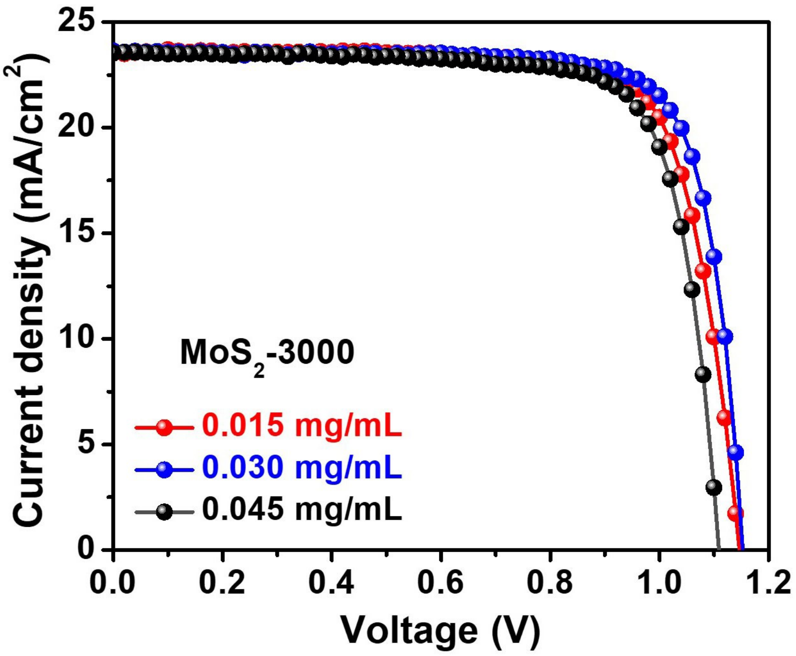

Fig. S11 The current density-voltage (J-V) curves of PSCs under different MoS$_2$-3000 nanosheets modifying amounts.

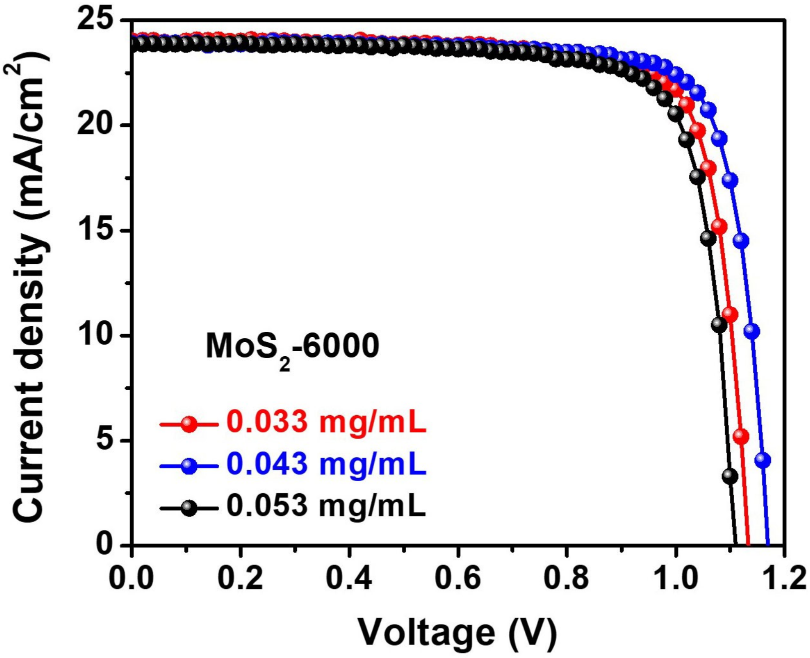

Fig. S12 J-V curves of PSCs under different MoS$_2$-6000 nanosheets modifying amounts.

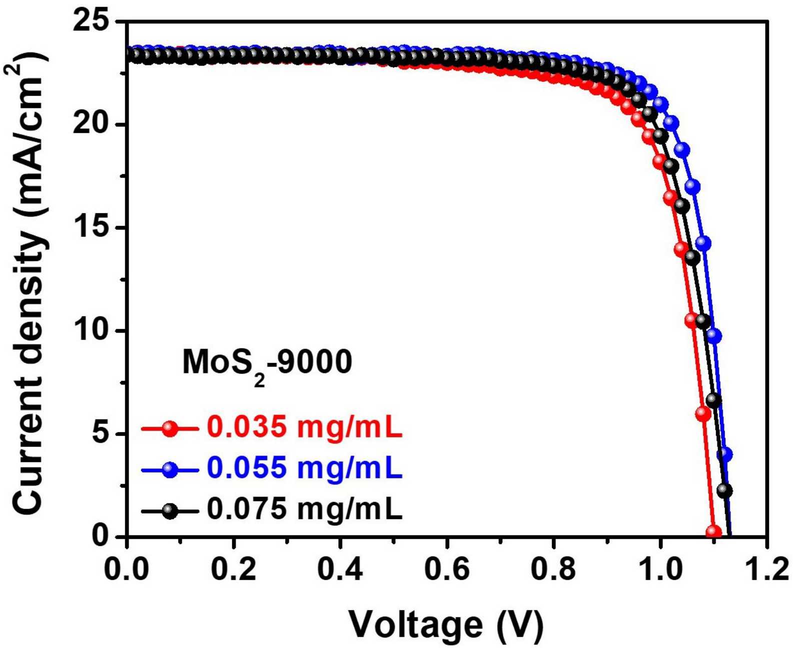

Fig. S13 J-V curves of PSCs under different MoS_2-9000 nanosheets modifying amounts.

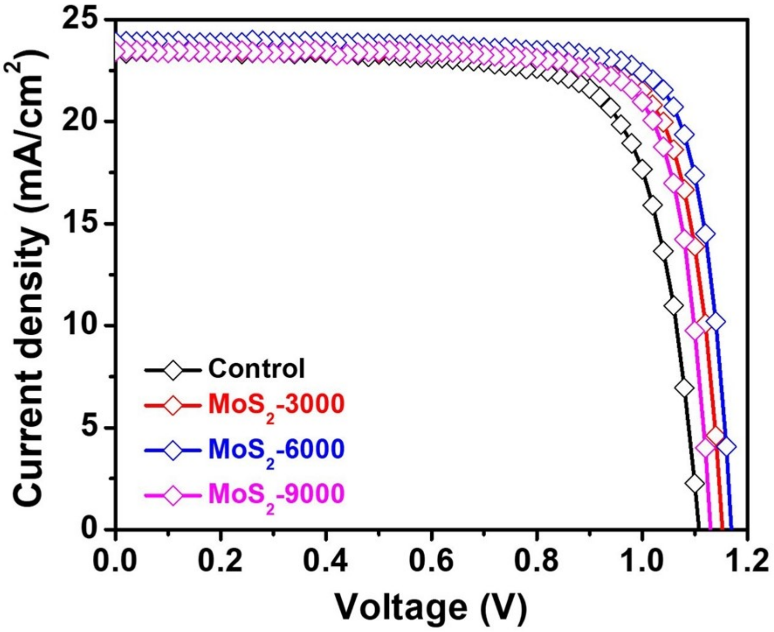

Fig. S14 J-V curves of champion PSCs with control perovskite and perovskite modified with MoS$_2$-3000, MoS$_2$-6000, and MoS$_2$-9000 nanosheets.

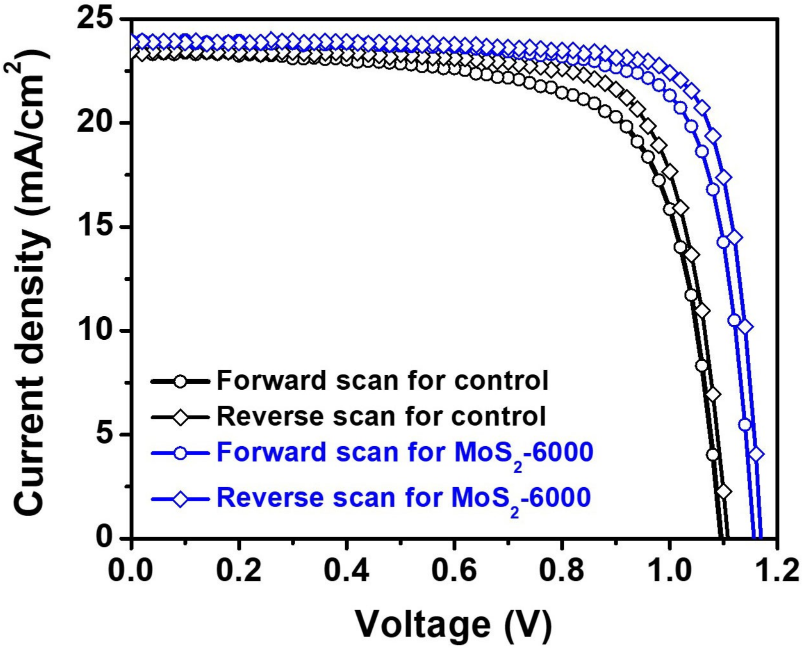

Fig. S15 J-V curves of the champion device with and without MoS$_2$-6000 nanosheets in both forward and reverse scan direction.

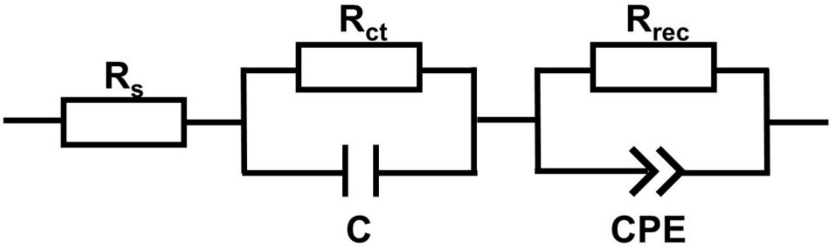

Fig. S16 Equivalent circuit of PSCs used for fitting impedance data.

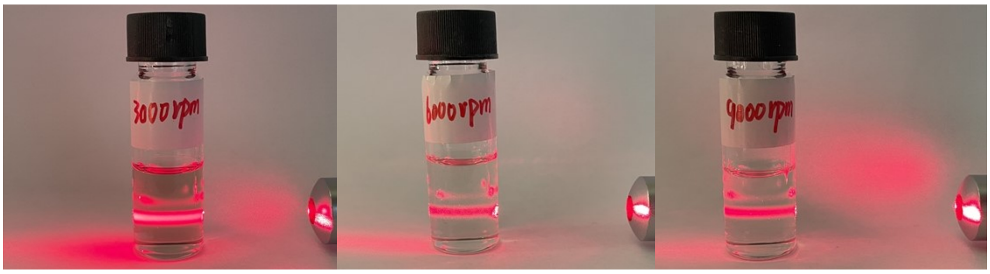

Figure S17 The Tyndall effect of the well-dispersed MoS_2 solutions with concentration of 1 mg/mL.

Table S1 The peak parameters and assignments of Pb 4f XPS for control perovskite and MoS_2-6000 modified perovskite film.

Samples	Elements	Binding energy/eV	Affiliation
Control	Pb 4f	138.20 / 143.00[a)]	[5,6]
	I 3d	619.00 / 630.50[b)]	[7,8]
MoS_2-6000	Pb 4f	138.39 / 143.29[a)]	[9,10]
	I 3d	619.19 / 630.69[b)]	[8,11]

a) (Pb $4f_{7/2}$ / Pb $4f_{5/2}$); b) (I $3d_{5/2}$ / $3d_{3/2}$)

Table S2 The detailed photovoltaic parameters of PSCs incorporating with MoS_2 that have been prepared at different centrifuge speeds and modifying amounts.

Centrifuge speed / rpm	Modifying amounts / (mg mL^{-1})	V_{oc} / V	J_{sc} / (mA cm $^{-2}$)	FF / %	PCE /%
	0.015	1.14	23.68	77.59	20.94
MoS_2-3000	0.030	1.14	23.63	79.86	21.51
	0.045	1.10	23.57	78.23	20.28
	0.033	1.12	24.08	80.56	21.72
MoS_2-6000	0.043	1.16	23.99	80.84	22.50
	0.053	1.10	23.93	79.46	20.92
	0.035	1.10	23.47	75.93	19.61
MoS_2-9000	0.055	1.12	23.49	80.35	21.14
	0.075	1.12	23.38	77.92	20.41

Table S3 The detailed photovoltaic parameters of champion PSCs with or without MoS_2.

Device	Scan	V_{oc} / V	J_{sc} / (mA cm^{-2})	FF / %	PCE / %	Integrated J_{sc} / (mA cm^{-2})
Control	Reverse	1.10	23.48	75.53	19.51	22.81
	Forward	1.08	23.40	72.25	18.26	
MoS_2-6000	Reverse	1.16	23.99	80.84	22.50	23.63
	Forward	1.14	23.99	78.17	21.37	

Table S4 The fitting parameters for the time resolved PL curves of perovskite films.

Samples	τ_{avg} (ns)	τ_1 (ns)	τ_2 (ns)	τ_3 (ns)	A_1 (%)	A_2 (%)	A_3 (%)
Control	180.69	180.61	180.71	180.76	33.33	33.33	33.34
MoS_2-6000	77.98	0.12	5.47	78.98	0.11	16.52	83.37

$F(t)=A_1\exp(-t/\tau_1)+A_2\exp(-t/\tau_2)+A_3\exp(-t/\tau_3)+\gamma_0$

where τ_1, τ_2, and τ_3 are fast decay time, intermediate decay time, and slow decay time, A_1, A_2, and A_3 are the coefficient, respectively.

Table S5 The related parameters fitted from the equivalent circuit for EIS spectra measurement.

Device	R_s/Ω	R_{ct}/Ω	C/nF	R_{rec}/Ω	CPE/nF
Control	133.8	14140	2.409E-8	8.782E5	1.718E-6
MoS_2-6000	39.41	8618	1.702E-8	1.831E6	1.891E-6

Table S6 The previously reported performances of PSCs devices decorated with MoS_2 nanomaterials prepared by different methods.

Method[a]	Function[b]	Device Structure	V_{oc} (V)	J_{sc} (mA/cm^2)	FF/%	PCE /%	Ref.
LPE	ABL	FTO/c-TiO_2/m-TiO_2/$MAPbI_3$/MoS_2 /Spiro-OMeTAD/Au	0.938	21.09	66.21	13.09	12
CVD	HTL	ITO/MoS_2/$CH_3NH_3PbI_{3-x}Cl_x$/PCBM /BCP /LiF/Al	0.96	14.89	67	9.53	13
LPE	ETL	ITO/TiO_2: MoS_2/$MAPbI_3$/Au	0.65	13.36	51	4.43	14
LPE	HTL	ITO/PEDOT:PSS/MoS_2-PAS/$MAPbI_3$ /PCBM/Ag	0.998	24.035	68.6	16.47	15
LPE	HTL	ITO/MoS_2/$MAPbI_3$/PCBM/Al	0.84	12.6	57	6.01	16
LPE	HTL	ITO/MoS_2/$MAPbI_{3-x}Cl_x$/C_{60}/BCP/Al	0.88	20.94	77.9	14.35	17
LPE	HTL	ITO/PTAA/MoS_2/$MAPbI_{3-x}Cl_x$/PCBM/PFN/Al	1.011	20.71	78.41	16.42	18
LPE	HTL	FTO/c-TiO_2/m-TiO_2/$MAPbI_3$/MoS_2:f-rGO/Spiro-OMeTAD/Au	1.11	22.81	79.75	20.12	19
Purchase	HTL	ITO/PEDOT: PSS-MoS_2/$MAPbI_3$/PCBM /BCP/Ag	0.952	20.7	72.3	14.2	20
TE	HTL	ITO/PEDOT:PSS/GO:PEG/$MAPbI_3$ /PCBM/MoS_2/Ag	1.135	22.834	73.8	19.14	21
Purchase	HTL	ITO/PEDOT:PSS-MoS_2/ $CH_3NH_3PbI_{3-x}Cl_x$/PCBM:Bphen/Ag	1.01	21.3	71.5	15.4	22
MALTS	ETL	FTO/MoS_2/$MAPbI_3$/Sipro-OMeTAD/Au	0.89	21.7	63.8	13.14	23
LPE	ABL	FTO/c-TiO_2/m-TiO_2/CsFAMAPbIBr/fMoS_2/Spiro-OMeTAD/Au	10.46	173.78	60.09	13.4	24
LPE	HTL	ITO/PTAA/MoS_2/$MAPbI_3$/PCBM /BCP/Ag	1.13	22.66	80.26	20.55	25
LPE	HTL	ITO/c-TiO_2/m-TiO_2/$MAPbI_{3-x}Cl_x$ /MoS_2/P3HT/Au	0.53	21.3	64	7.2	26
HM	HTL	FTO/TiO_2/$MAPbI_3$/Spiro-OMeTAD: MoS_2/MoO_3/Ag	1.10	24.48	75	20.18	27
LPE	ABL	ITO/PEDOT:PSS/MoS_2 /$MAPbI_3$:MoS_2 /PCBM/Bphen/Ag	1.02	22.28	77.91	18.31	28
CVD	HTL	co-GR/MoS_2/$MAPbI_3$/PCBM/BCP/Al	0.88	19.97	74.46	13.09	29
CVD	ETL	TETA-GR/MoS_2/$MAPbI_3$/PTAA/Au	0.92	20.3	76.4	14.27	30

References

1 M. Birkholz, Thin Film Anal. by X-Ray Scatt., https://www.wiley.com/en-mx/Thin+Film+Analysis+by+X+Ray+Scattering-p-9783527310524, (accessed 16 July 2021).

2 N. Rolston, K. A. Bush, A. D. Printz, A. Gold-Parker, Y. Ding, M. F. Toney, M. D. McGehee and R. H. Dauskardt, *Adv. Energy Mater.*, 2018, **8**, 1802139.

3 S. Sun, Y. Fang, G. Kieslich, T. J. White and A. K. Cheetham, *J. Mater. Chem. A*, 2015, **3**, 18450–18455.

4 J. Feng, *APL Mater.*, 2014, **2**, 081801.

5 L. R. Pederson, *J. Electron Spectros. Relat. Phenomena*, 1982, **28**, 203–209.

6 M. E. Ekman, J. W. Anderegg and G. L. Schrader, *J. Catal.*, 1989, **117**, 246–257.

7 F. Solymosi and I. Kovács, *Surf. Sci.*, 1993, **296**, 171–185.

8 C. Furlani, G. Mattogno, G. Polzonetti, R. Barbieri, E. Rivarola and A. Silvestri, *Inorganica Chim. Acta*, 1981, **52**, 23–28.

9 D. S. Zingg and D. M. Hercules, *J. Phys. Chem.*, 1978, **82**, 1992–1995.

10 A. Osaka, Y. H. Wang, Y. Miura and T. Tsugaru, *J. Mater. Sci.*, 1991, **26**, 2778–2782.

11 H. Moers, H. Klewe-Nebenius, G. Pfennig and H. J. Ache, *Fresenius' Zeitschrift für Anal. Chemie*, 1987, **329**, 361–366.

12 A. Capasso, F. Matteocci, L. Najafi, M. Prato, J. Buha, L. Cinà, V. Pellegrini, A. Di Carlo and F. Bonaccorso, *Adv. Energy Mater.*, 2016, **6**, 1600920.

13 Y. G. Kim, K. C. Kwon, Q. Van Le, K. Hong, H. W. Jang and S. Y. Kim, *J. Power Sources*, 2016, **319**, 1–8.

14 M. I. Ahmed, Z. Hussain, A. Khalid, H. M. N. Amin and A. Habib, *Mater. Res. Express*, 2016, **3**, 045022.

15 R. Dai, Y. Wang, J. Wang and X. Deng, *ChemSusChem*, 2017, **10**, 2869–2874.

16 U. Dasgupta, S. Chatterjee and A. J. Pal, *Sol. Energy Mater. Sol. Cells*, 2017, **172**, 353–360.

17 P. Huang, Z. Wang, Y. Liu, K. Zhang, L. Yuan, Y. Zhou, B. Song and Y. Li, *ACS Appl. Mater. Interfaces*, 2017, **9**, 25323–25331.

18 G. Kakavelakis, I. Paradisanos, B. Paci, A. Generosi, M. Papachatzakis, T. Maksudov, L. Najafi, A. E. Del Rio Castillo, G. Kioseoglou, E. Stratakis, F. Bonaccorso and E. Kymakis, *Adv. Energy Mater.*, 2018, **8**, 1702287.

19 L. Najafi, B. Taheri, B. Martín-García, S. Bellani, D. Di Girolamo, A. Agresti, R. Oropesa-Nunìez, S. Pescetelli, L. Vesce, E. Calabrò, M. Prato, A. E. Del Rio Castillo, A. Di Carlo and F. Bonaccorso, *ACS Nano*, 2018, **12**, 10736–10754.

20 D. Wang, N. K. Elumalai, M. A. Mahmud, H. Yi, M. B. Upama, R. A. Lee Chin, G. Conibeer, C. Xu, F. Haque, L. Duan and A. Uddin, *Synth. Met.*, 2018, **246**, 195–203.

21 Y. Wang, S. Wang, X. Chen, Z. Li, J. Wang, T. Li and X. Deng, *J. Mater. Chem. A*, 2018, **6**, 4860–4867.

22 H. K. Lin, J. X. Li, H. C. Wang, Y. W. Su, K. H. Wu and K. H. Wei, *RSC Adv.*, 2018, **8**, 12526–12534.

23 R. Singh, A. Giri, M. Pal, K. Thiyagarajan, J. Kwak, J. J. Lee, U. Jeong and K. Cho, *J. Mater. Chem. A*, 2019, **7**, 7151–7158.

24 A. Agresti, S. Pescetelli, A. L. Palma, B. Martín-García, L. Najafi, S. Bellani, I. Moreels, M. Prato, F. Bonaccorso and A. Di Carlo, *ACS Energy Lett.*, 2019, **4**, 1862–1871.

25 G. Tang, P. You, Q. Tai, A. Yang, J. Cao, F. Zheng, Z. Zhou, J. Zhao, P. K. L. Chan and F. Yan, *Adv. Mater.*, 2019, **31**, 1807689.

26 R. Ray, A. S. Sarkar and S. K. Pal, *Sol. Energy*, 2019, **193**, 95–101.

27 L. L. Jiang, Z. K. Wang, M. Li, C. H. Li, P. F. Fang and L. S. Liao, *J. Mater. Chem. A*, 2019, **7**, 3655–3663.

28 Z. Liu, K. Liu, F. Zhang, S. M. Jain, T. He, Y. Jiang, P. Liu, J. Yang, H. Liu and M. Yuan, *Sol. Energy*, 2020, **195**, 436–445.

29 D. H. Shin, S. H. Shin and S. H. Choi, *Appl. Surf. Sci.*, 2020, **514**, 145880.

30 D. H. Shin, J. S. Ko, S. K. Kang and S. H. Choi, *ACS Appl. Mater. Interfaces*, 2020, **12**, 4586–4593.